Draft

Unidirectional wicking-driven flow boiling on tilted pillar structures for high-power applications

Wei-Ting Hsu[*], Namkyu Lee[†], Maroosol Yun[*], Donghwi Lee[#], and Hyung Hee Cho[*,‡]

* Department of Mechanical Engineering, Yonsei University, 50 Yonsei-ro, Seodaemun-gu, Seoul 120-749, Korea

[†]IBI-4, Forschungszentrum Jülich GmbH, D-52428 Jülich, Germany

Division of Mechanical System Engineering, Jeonbuk National University, 567 Baekje-daero, Deokjin-gu, Jeonju-si, Jeollabuk-do, Republic of Korea 54896

‡Corresponding author: hhcho@yonsei.ac.kr (H. H. Cho)

Abstract

Energy management issues of high-power units become serious because of the miniaturization of electronic components; the heat flux of heated surfaces can rise above 250 W/cm^2. The cooling systems typically result in considerable energy consumption for ensuring its cooling efficiency; to prevent the system failure, power plants require generating more electric power, feeding the amount of carbon dioxide into the environment and thus worsens global warming.

Among cooling methods applying in industrial fields, boiling heat transfer is the most potential cooling method for resolving energy consumption issues accompanied by climate change. The overall boiling heat transfer performance is significantly enhanced by augmenting the capillary wicking within structured surfaces for ensuring the surface coolant supply.

Of wicking characteristics in boiling heat transfer, polymerized surfaces with bending pillar arrays can guide bulk liquid in the direction of interest. This unique wicking characteristic significantly enhances surface wickability when liquid propagation corresponds with the pillar tilted direction. In this study, we first experimentally investigated the effect of the polymerized pillar surface regarding wicking direction on heat transfer under subcooled flow boiling conditions (40 K). When the pillar deflection was toward the direction of liquid propagation (compared to against the flow direction), the unidirectional wicking enhanced the critical heat flux (CHF) by 6–31%, showing a strong directional dependence. Experimental results could optimize the design of anisotropic wicking surfaces for enhancing boiling heat transfer.

Keywords:

Anisotropic wicking surface; Unidirectional wicking; Polymerized pillar arrays; Pillar tilting direction; Subcooled flow boiling; Energy consumption management

Nomenclature

A	=	Heated area (m^2)
d	=	Pillar diameter (μm)
F_d	=	Liquid driving force (N)
F_p	=	Liquid pinning force (N)
h	=	Heat transfer coefficient ($W/m^2 \cdot K$)
I	=	Imported current (A)
k	=	Thermal conductivity (W/m·K)
L	=	Length (m)
l	=	Thickness (μm)
l_w	=	Wicking distance (mm)
P	=	Pillar spacing (μm)
Q	=	Total input heat (W)
q	=	Heat flux (W/m^2)
q_{loss}	=	Heat loss (W/m^2)
Re	=	Reynolds number
s	=	Solid fraction
T	=	Temperature (°C)
t	=	Time (s)
V	=	Imported voltage (V)
W	=	Wicking coefficient ($mm/s^{0.5}$)

Greek letters

α	=	Advancing contact angle (°)
β	=	Receding contact angle (°)
γ	=	Linear fraction of contact line
θ	=	Static contact angle (°)

ϑ	=	Perpendicular spacing (μm)
φ	=	Pillar tilt angle (°)

Subscripts

a	=	Advancing
c	=	Contact
d	=	Driving
e	=	Entrance
f	=	Fluid
h	=	Hydraulic
o	=	Intrinsic
p	=	Pinning
R	=	RTD sensor
r	=	Receding
s	=	Surface
si	=	Silicon
W	=	Heated wall

1. Introduction

Recently, energy management issues of supercomputers, refrigerators, and electronic devices have become seriously owing to the miniaturization of electronic components; the heat flux of heated surfaces can rise above 250 W/cm^2. To release such heat, the cooling systems typically result in considerable energy consumption to ensure cooling efficiency [1-2]. In this regard, power plants generate more electric power to prevent system failure, while an amount of carbon dioxide feeds into the environment, accelerating global warming (particularly for thermal power plants) simultaneously. Hence, the cooling mechanisms of high-power units must efficiently transmit heat energy from target surfaces to stabilize climate change.

Among the cooling methods applied in industrial fields, heat dissipation capacities of heated surfaces releasing heat via phase change (approach 80,000 W/m^2·K) are significantly higher than those with single-phase cooling (below 10000 W/m^2·K) [3]. Thus, the phase-change heat transfer mechanism is the most potential cooling method for resolving energy consumption issues accompanied by global warming.

In phase-change heat transfer, boiling heat transfer is the high-efficient cooling method for high-power units. The overall boiling heat transfer performance is significantly enhanced by ensuring the surface coolant supplied capacity associated with structured surfaces' wicking characteristics. Water can be directionally repelled or imbibed on biologically inspired surfaces having micro-/nanostructures via capillary pumping (interfacial wicking) [4-5]. Of the capillary wicking, biological surfaces (the lotus leaf, butterfly wings, and insect exoskeletons) inspired researchers to create micro/nano-wicked structures, generating energy gradients exhibiting beneficial wicking characteristics. Apart from surface topography, chemical modification of patterned surfaces also contributes to surface wettability by coating with thin hydrophilic or hydrophobic layers, respectively [6-7].

The wicking characteristics of structured surfaces reflect the rewetting capacity on heated surfaces and greatly enhance boiling heat transfer. Partial dry-out of heated surfaces develops as vapor bubbles form vigorously on heated walls where surface rewetting is relatively low compared to the evaporation rate. Consequently, a vapor film appears on surfaces engaging in heat transmission, creating a sudden transition to a boiling crisis (i.e., the heat flux attains a critical heat flux [CHF] [8-9] because of low liquid supply). This detrimental effect on boiling heat transfer can be prevented by improving the rewettability of the heated surface, thus delaying film boiling. On the other hand, enhancement of surface hydrophobicity

augments heat dissipation; hydrophobic surfaces exhibit high heat transfer coefficients (HTCs) attributable to active bubble agitation in the superheated evaporative layer during low heat flux [10-11]. However, a hydrophobic surface is very prone to premature dry-out due to its poor wickability that compromises the rewetting of the heated surface.

The influence of surface topography (the wicking characteristics) on boiling heat transfer has been experimentally explored [12-18]. Wen et al. [12] created surfaces of Cu-woven micro-meshes (one or more layers) to explore pool boiling heat transfer. When the number of microlayers increased, the overall CHF and HTC enhanced significantly due to the improved capillary pumping, indicating that the surface wicking characteristics dominated boiling heat transfer. The effects of capillary pumping on boiling heat transfer have also been observed on surfaces with nanopillar [13-15] and micropillar [16-18] arrays. Wang et al. [15] experimentally examined the effect of microchannels (with nanowires) on two-phase boiling under forced convective subcooling conditions (30 K); the microchannels significantly improved capillary pumping compared to that of the plain surface. Similarly, two-phase heat transfer improved when capillary flow was enhanced by hierarchical wicking structures [17]. The surfaces consisted of micropillars of various configurations with super-hydrophilic nano-nickel coatings. Compared to nonwetting flat surfaces, micro-/nano-pillar surfaces exhibited notable improvements in capillary wicking, showing that this was enhanced by manipulating the surface roughness and the geometry. In brief, enhancement of two-phase boiling is directly associated with enhanced capillary pumping afforded by micro-/nano-structured surfaces. This facilitates surface rewetting during nucleate boiling.

Liquids may spread isotopically (in all directions) on a surface, but an anisotropic wicking surface can drive liquid in the direction of the surface energy gradient on artificial surfaces; wicking then exhibits a strong directional dependence called *unidirectional wicking*. Several studies have investigated liquid propagation on micro-structured surfaces featuring tunable micro-wrinkles [19-20], chemical stripes [21], microgrooves [22-24], and micropillars [25-26]. On surfaces featuring parallel hydrophilic and hydrophobic stripes [21], liquid moves in a direction perpendicular to the edge of the stripe patterns and not in the direction parallel to the pattern edge. Of note, water droplets moved along stripe-patterned surfaces exhibiting surface wettability gradients when the hydrophobic:hydrophilic stripe width ratio was reduced. Their results showed that the spread is anisotropic and chemical surface modification can strengthen the unidirectional wicking. On micropillared surfaces, water droplets move in the direction of pillar tilting, generating the unidirectional wicking. Chu et al. [25] deposited thin

gold layers of various thicknesses on the surfaces of silicon nanopillars tilted from 2 to 52° and experimentally evaluated the liquid spreading. When a droplet was placed on a surface, the droplet moved in the direction of nanopillar deflection, indicating that interfacial wicking can be enhanced by guiding liquid in a single direction via manipulation of the surface topography.

As mentioned above, the unidirectional wicking is often observed on surfaces with anisotropic wicking structures, including chemical gradients and structural micropillar arrays made of polymers. The effects of such surfaces on flow boiling have not been experimentally investigated. We first experimentally explored the effects of anisotropic wicking surfaces on the wicking direction during flow boiling under subcooled conditions (40 K). The surfaces featured bent pillars spaced at 250 and 500 μm. A 200-nm-thick hydrophilic layer was uniformly deposited on pillar surfaces to further augment surface wickability. We determined the effect of the relative wicking direction on boiling heat transfer by analyzing wicking per se and the relationship between the liquid pinning and driving forces (Fig. 1).

2. Materials and Methods

2.1 Fabrication of anisotropic wicking surfaces with tilted pillars

The fabrication process of the test surfaces is shown in Fig. 2(a). We used Polydimethylsiloxane (PDMS) materials to create vertical PDMS pillar arrays on silicon substrates based on a 2-step replica modeling method [27-29]. First, silicon molds composed of vertical pillar arrays were coated with a 200-nm release agent (parylene C) for reducing the adhesion of PDMS materials. Subsequently, PDMS solutions with a mixed ratio of 10:1 were poured on the silicon molds and cured at 80℃ for 7 hours in a convection oven; PDMS stamps composed of various circular cavities with 250 um and 500 um spacings were created after peeling off the cured PDMS part from the silicon mold.

Next, the 200 nm release agent was uniformly coated on the PDMS stamps using an e-beam evaporator (KIST, Korea), and the prepared PDMS solution (10:1) was poured on the PDMS stamps; here, a sharp surgy knife was used to remove the excess PDMS. After that, the PDMS stamps were vertically placed on a silicon substrate and pressed by metal blocks with a total weight of 2 kg following the same curing procedure. Consequently, surfaces consisted of vertical PDMS pillars and silicon substrates were fabricated by removing the PDMS stamps from the silicon surface.

Figure 2(b) shows the pillar tilting process on a surface with vertical PDMS pillars. After curing at 80°C for 7 hours, the surface was laid on a quartz plate in a sputter coater at a fixed angle of 45°. One side of each pillar was gold-coated (200-nm in thickness) at 0.267 nm/s; the pillars were thus tilted by an average angle (φ) of 30°. Subsequently, the entire pillar surface was uniformly coated with 200 nm of SiO_2 to chemically strengthen unidirectional wicking [Fig. 2(c)].

In general, surface rewetting can be directly evaluated by measuring apparent surface contact angles (CAs), as discussed in the next section.

2.2 Surface wettabilities of surfaces with chemical coatings

Figure 3(a) shows a PDMS stamp placed vertically on a silicon substrate; the stamp is composed of vertical pillar arrays with variations in pillar spacing. We evaluated the bases of test surfaces because it was difficult to measure the thicknesses of chemical coatings on deflected PDMS pillars. A thin PDMS membrane (average thickness 200 nm) remained between the pillar arrays and the silicon substrate; herein, the average thickness of the SiO_2 and gold hydrophilic coatings were approximately 200 nm which was estimated via scanning electron microscopy (SEM) [Fig. 3(b) and (c)]. Notably, an additional 20-nm-gold layer was further deposited on the hydrophobic pillar surfaces after bending treatments to ensure the homogeneity. The configurations of the anisotropic wicking surfaces are summarized in Table 1, where the pillar diameter (d) and length (L) were 50 and 300 μm respectively, with spacings of 250 and 500 μm between neighboring pillars.

The apparent surface CAs on test surfaces are shown in Fig. 3(d); all measurements were conducted by depositing 5-μL droplets onto the surfaces, followed by drop shape analysis (DSA100 instrument; Krüss, Hamburg, Germany). As the results, anisotropic wicking surfaces with hydrophilic coatings evidenced high wettability; the CAs were $5 \pm 0.6°$ and $10 \pm 1.1°$ for the surfaces of deflecting pillars spaced at 250 and 500 μm, respectively. In contrast, the apparent CAs on hydrophobic surfaces with such spacings were $141 \pm 2.1°$ and $122 \pm 2.2°$ respectively, indicating that hydrophilic coatings greatly enhanced surface rewetting, and thus (possibly) boiling heat transfer. Next, we will discuss the data reduction required.

2.3 Experimental setup and procedure

We used four systems of equipment when investigating how unidirectional wicking affected boiling heat transfer: a water supply, a flow chamber, a heater, and a data recorder [Fig.

4(a)]. The working fluid was deionized water (18.2 MΩ/cm) held in a 44-L tank with a pressure valve at the top. An immersion heater (Hanil Industrial Machine Co., Gwangju, Korea) was used to maintain the fluid at 100°C for 2 hours (this removed all gas and contaminants). The inlet temperature of the working fluid was held at 59.3 ± 0.4°C by a heater (model 131001694) within the closed-loop system and pumped into the flow chamber by a magnetic pump (TXS5.3 or SUS316; Tuthil Co., Burr Ridge, IL, USA) and an electric motor (LG-OTIS 3,500 rpm, Korea). A flow meter (Ultra Mass MK II, Tokyo, Japan) detected the mass flow rate of the working fluid (which was maintained at 0.51 kg/min). The flow chamber was a rectangular channel, 5 mm in both length and width (D_h = 5 mm) constructed from polyetheretherketone (PEEK) with low thermal conductivity (k = 0.25 W/m-K). Bubbles on test surfaces were observed through two quartz windows on the side of the flow chamber. The length of the upstream flow chamber (L_e) was longer than that required to generate a fully developed flow before the working fluid reached the test surfaces. The Reynolds number was 3,600 and the required length was thus 86.13 mm based on $4.4 \cdot Re^{1/6} \cdot D_h$.

For heating, a direct current (DC) power supply (300 V-10 A; KSC, Korea) was connected to copper bus bars below the test surfaces to produce heat by importing different rated powers; herein, an 800-nm indium tin oxide (ITO) layer was deposited on resistance temperature detected sensors (RTDs) as a thin film heater. The heated area of each RTD was 5 mm in width and 10 mm in length. Upon the ITO coated layer, 100-nm Au layers were further deposited on the heater surface for stabilizing the electric current supply during the experiments, as shown in Fig. 4(b) and (c). A high-conductivity silver paste (electrical resistivity 10^{-4} Ω-cm) was used to reduce the contact resistances of surfaces between the copper bus bar and the electrodes of the resistance temperature detector (RTD) sensors.

Furthermore, the data-recording equipment included the RTD sensors, a signal module, a data recorder (model 3490A; Agilent Technologies, Santa Clara, CA, USA), and K-type thermocouples (Omega Engineering, Stamford, CT, USA). The working fluid was measured by K-type thermocouples placed at the inlet and outlet of the flow chamber; the temperature gradients of heated walls were detected using the RTD sensors during the experiments. All temperature data were collected and analyzed on a personal computer. Fig. 4(d) schematically depicts the location of temperature-measured components in the flow channel. More information on the experimental setup and fabrication of the RTD sensors was given in our previous studies [30-32].

3. Results and Discussion

3.1 Boiling heat transfer characteristics on anisotropic wicking surfaces

Figure 5(a) and (b) show the boiling characteristics of various test surfaces under subcooled flow boiling (40 K). The mass flow rate was 0.51 kg/min (Re = 3,600). A surface with a 200-nm-thick PDMS membrane served as the reference when examining the influence of the unidirectional wicking on wicking direction during boiling heat transfer. Hydrophilic, anisotropic wicking surfaces (pillar tilt angle 30°) varying in terms of pillar spacing improved the CHF (to 210–248 W/cm^2) compared to the bare PDMS surface (185 W/cm^2). However, a test surface without the SiO_2 coating exhibited a similar trend (113–148 W/cm^2) compared to a hydrophobic, bare PDMS surface, indicating that the boiling crisis was effectively delayed by the unidirectional wicking and that CHF enhancement could be further increased by chemical coating of a hydrophilic layer to strengthen surface rewetting.

Generally, the spacing between pillar arrays affects the capillary pumping within pillars; the cooling liquid must pass through heated surfaces for delaying the CHF [33-34]. This was observed when wicking was anisotropic; hydrophilic surfaces of deflected PDMS pillars spaced at 250 μm exhibited a higher CHF (by 9–11%) than did surfaces with pillars spaced at 500 μm. The influence of pillar spacing on the CHFs of hydrophobic surfaces was insignificant.

Notably, significant CHF enhancement of the unidirectional wicking was observed when pillar deflection was toward rather than against the flow. Hydrophobic anisotropic wicking surfaces remarkably improved the CHF (by 29–31%) compared to surfaces composed of pillars deflected against the flow. In contrast, hydrophilic surfaces with the anisotropic wicking structures did not significantly improve the CHF, which increased by only 6–9% compared to that of surfaces with pillars deflected against the flow. The differences in CHF enhancement between hydrophobic and hydrophilic anisotropic wicking surfaces are attributable to the chemical hydrophilic layers, which improved surface wettability but reduced the difference between the relative and mainstream wicking directions during boiling heat transfer. In other words, the overall boiling heat transfer performance under subcooled flow (40 K) was simultaneously dominated by surface wettability, pillar spacing, and the tilts of the deflecting

pillars of anisotropic wicking surfaces. The pillar deflection maximally affected flow boiling.

Figure 5(c) shows the HTCs for various test surfaces and reflects the effects of surface wettability, pillar spacing, and pillar deflection. The relative heat flux on test surfaces was approached the boiling crisis. First, the overall HTCs were higher on anisotropic wicking surfaces than on bare PDMS surfaces; the enhancements were 14–63% and 8–29% for hydrophilic and hydrophobic surfaces, respectively. The improved HTCs were significantly higher on hydrophilic surfaces than on hydrophobic surfaces; enhanced surface wettability both delayed the CHF and extended the HTC. Reduced spacing between deflected pillars increased the HTCs of anisotropic wicking surfaces, referable to more active bubble nucleation on surfaces with narrow rather than wide spaces between deflecting pillars. Here, the bubble characteristics of hydrophilic surfaces having bending pillars spaced at 250 μm and 500 μm are shown in supplementary materials.

The local HTCs of surfaces with pillars deflected along the flow direction were significantly higher than those of surfaces with pillars that opposed convective flow; by 25–28% and 20–36% for hydrophilic and hydrophobic surfaces, respectively. The experimental HTC data supported an earlier suggestion that boiling heat transfer under subcooled flow boiling (40 K) was mainly dominated by the unidirectional wicking in terms of pillar deflection.

Turning to the effect of surface wettability on anisotropic wicking surfaces, the relationship between the apparent CAs and the CHFs of the various test surfaces is discussed in the next section.

3.2 Influence of the surface wettability of anisotropic wicking surfaces on the CHF

Figure 6 shows the CHFs as functions of the measured CAs for the various test surfaces; the experimental results were compared to those of a CHF model that considered the effect of surface wettability on flow boiling [35]. The most direct means of surface wettability evaluation is via measurement of the surface CAs of hemispherical water droplets placed on test surfaces. Generally, wettability can be divided into two types depending on the surface CAs, thus that of hydrophilic (CA = 0–90°) and hydrophobic (CA = 90–180°) surfaces.

Accordingly, the overall CHFs of test surfaces decreased as the surface changed from hydrophilic to hydrophobic, in agreement with the CHF versus surface CA variations proposed in [35]. The decreasing CHF reflected principally the fact that low surface wettability compromised the rewetting associated with a sudden transition of film boiling. Notably, anisotropic wicking surfaces with the same pillar configurations exhibited different CHF values

although the measured surface CAs did not change. In particular, the CHF of anisotropic wicking surfaces fell when the pillars were tilted against convective flow, indicating that surface rewetting was dominated by the relative wicking direction. We measured various wicking characteristics to determine the effect of unidirectional wicking on surface rewetting.

3.3 Effect of pillar tilt direction on wicking characteristics

Figure 7(a) shows the wicking characteristics of the hydrophilic anisotropic wicking surfaces. Before measuring wicking, the direction of the deflecting pillars was perpendicular to the container filled with DI water. We tested wicking by gradually moving the test plate downward until it attained the water surface and recorded wicking using the high-speed camera. Hydrophilic test surfaces were considered representative when determining wicking characteristics because hydrophobic surfaces did not exhibit significant wicking. When anisotropic surfaces contacted the DI water, bulk water flowed vertically toward the top of each test surface, powered by capillary pumping. Surfaces on which the deflecting pillars were spaced at 250 μm exhibited longer wicking than did those with pillars spaced at 500 μm, from 0 to 0.1 s. Thus, surface wickability improved on narrowing of the spacing between pillars.

Apart from this spacing effect, pillar direction influenced wicking characteristics. From 0 to 0.1 s, bulk water passed through half of the test surface with a pillar spacing of 250 μm when wicking was in the direction of pillar deflection. In contrast, only a little water flowed when wicking was against the direction of pillar tilt. The flow behaviors on surfaces with pillars spaced at 500 μm were similar, indicating that strong pinning forces developed when the pillars were tilted against the direction of liquid propagation.

Figure 7(b) shows the average wicking velocities for the various test surfaces. These were given by $W = l_w/t^{0.5}$, where W is the wicking coefficient, which representing the wicking velocity, l_w is the wicking distance, and t is the liquid propagation time [36]. The overall wicking velocities of surfaces with deflecting pillars spaced at 250 μm (16.4 and 21.6 mm/s$^{0.5}$) were significantly higher than those of surfaces with pillars spaced at 500 μm (5.8 and 9.5 mm/s$^{0.5}$); the results showing that the surface rewetting capacity was enhanced by narrowing the pillar spacing. On the other hand, the wicking velocity increased when the pillars were tilted towards the direction of liquid propagation compared to those surfaces against the flow direction of bulk water by 32 and 64% for surfaces with spacings of 250 and 500 μm.

These experimental observations indicated that the surface wickability of hydrophilic

anisotropic surfaces could be improved both by narrowing the between-pillar spacing and varying pillar deflection. Surface-rewetting improved significantly when the pillars were deflected toward the direction of liquid propagation; the pillars augmented capillary pumping by generating unidirectional wicking along with the convective flow, as shown in Fig. 8. This enhanced the overall boiling heat transfer performance under subcooled flow conditions (40 K), in line with the experimental results.

3.4 Effect of the F_{pin}:F_{rel} force ratio and the wicking direction on surface rewetting

Enhancements of both the HTC and CHF of anisotropic wicking surfaces were experimentally evident on bubble visualization and measurement of wicking characteristics, respectively. The underlying mechanism is the directional effect of deflecting pillars that generate various forces that pin and drive bulk liquid. These forces are the F_p and the F_d, which can be estimated using the model of Malvadkar et al. [37], who evaluated the wetting characteristics of water droplets on anisotropic wicking surfaces. It was experimentally shown that water droplets could be pinned on and released from surfaces of obliquely aligned polymerized pillars by varying the direction of pillar deflection. Thus, we estimated the liquid pinning and driving forces (F_p and F_d) on various test surfaces to explore the relationship between the direction of unidirectional wicking and the boiling heat transfer characteristics under 40 K-subcooled flow.

According to the previous work [37], the force ratio (F_p/F_d) on an anisotropic wicking surface can be approximately estimated using the intrinsic advancing CA (θ_a) and receding CA (θ_r) of a water droplet on test surfaces. Notably, the dynamic CAs used for force ratio estimating were determined from bare PDMS surfaces reflecting the dynamic CAs on surfaces composed of bending pillar arrays. Thus, we measured the dynamic CAs of water droplets on hydrophilic and hydrophobic bare PDMS surfaces by depositing 5-μL amounts on the test surfaces and recording behaviors using the high-speed camera, as shown in Fig. 9(a). In addition, we further measured the dynamic CAs on surfaces composed of bending pillar arrays spaced at 250 μm for determining the confidence of the predicted force ratios; herein, the hydrophilic-bending pillar surface with 250-μm spacing was selected as the representative case as shown in Fig. 9 (b). The images were analyzed with the aid of the DSA-100 drop shape analyzer; the results are given in Table 3.

The force ratio of the liquid pinning (F_p) and driving (F_d) forces is given by:

$$\frac{F_p}{F_d} = \frac{\cos\theta_{r,p} - \cos\theta_{a,p}}{\cos\theta_{r.d} - \cos\theta_{a,d}} \tag{7}$$

where $\cos\theta_{r,p}$ and $\cos\theta_{a,p}$ are the predicted receding and advancing CAs on test surfaces in the pinning direction when the pillar deflection opposes liquid propagation, and $\cos\theta_{r,d}$ and $\cos\theta_{a,d}$ are the predicted receding and advancing CAs on the same surfaces in the driving direction when the pillar deflection aids liquid propagation.

In the pinning direction, the predicted advancing ($\theta_{a,p}$) and receding ($\theta_{r,p}$) CAs are given by:

$$\theta_{a,p} = \gamma \cdot min(\pi, \alpha_o + \varphi) + (1-\gamma)\pi \quad (8)$$

$$\theta_{r,p} = \gamma \cdot (\beta_0 - \varphi) + (1-\gamma)\pi \quad (9)$$

where γ is the linear fraction of the contact line on the pillar surface, α_o and β_o are the measured advancing and receding CAs on a bare PDMS surface (i.e., both the hydrophilic and hydrophobic surfaces were measured, respectively), and φ is the pillar tilt angle. Herein, the linear fraction of the contact line (γ) is defined as:

$$\gamma = \pi s/2\{[1 + (\pi/2 - 1)s]\} \quad (10)$$

$$s = d/(d + \vartheta) \quad (11)$$

where s is the solid fraction, d is the pillar diameter, and ϑ is the perpendicular spacing between the pillars.

Conversely, in the driving direction, the predicted advancing ($\theta_{a,d}$) and receding ($\theta_{r,d}$) CAs are given by:

$$\theta_{a,d} = \gamma \cdot min[\pi, \max(\theta_{a1}, \theta_{a2})] + (1-\gamma)\pi \quad (12)$$

$$\theta_{r,d} = \gamma \cdot (\beta_o + \varphi - \pi/2) + (1-\gamma)\pi \quad (13)$$

where θ_{a1} is the predicted advancing CA as the leading edge of a droplet attains the neighboring pillar, and θ_{a2} is the predicted advancing CA as a droplet moves along the pillar array [37]. The advancing CAs (θ_{a1} and θ_{a2}) are defined by:

$$\theta_{a1} = 3\pi/2 - \varphi - \tan^{-1}(\cot\varphi/(1-s)) \quad (14)$$

$$\theta_{a2} = \alpha_o + \pi/2 - \varphi \quad (15)$$

The ratio of the liquid pinning to the driving forces on an anisotropic wicking surface was estimated by substituting the relevant parameters and the measured dynamic CAs on hydrophilic and hydrophobic bare PDMS surfaces into these equations. The variables for deflecting PDMS pillars were 50 μm for the diameter (d), 200 μm for the perpendicular distance between the pillars (ϑ), and 30° for the pillar tilt angle (φ), which were measured via

SEM images. Thus, the force ratios for surfaces with pillars spaced at 250 and 500 μm in the driving direction were approximately 0.52 and 0.53; those for hydrophobic surfaces were 0.57 and 0.58, respectively. Furthermore, the confidence of the force ratios was further determined using predicted dynamic CAs and actual dynamic CAs of bending pillar surfaces with 250-μm spacing, as shown in Fig. 9(c). The force ratio predicted using the actual dynamic CAs showed a well-agreement with those forces estimated with the predicted dynamic CAs, revealing a 95% confidence, accordingly.

Moreover, the predicted force ratio for an anisotropic wicking surface was also in good agreement with the experimental results of boiling heat transfer under subcooled flow conditions (40 K). Fig. 10 shows the relationship between the CHF and the predicted force ratio for various anisotropic wicking surfaces. In the driving direction, the hydrophilic surfaces exhibited CHF enhancements at lower force ratios than those of hydrophobic surfaces. However, CHF improvements on hydrophilic surfaces were also observed in the pinning direction, showing that the CHF was dominated by surface wettability. Narrowing the pillar spacing increased the CHF but did not significantly affect the predicted force ratio. The CHF improvement indicated that pillar spacing dominated the surface rewetting of hydrophilic surfaces by enhancing interfacial capillary pumping.

It is noteworthy that the overall CHFs of both hydrophilic and hydrophobic surfaces remarkably improved when the pillars were deflected toward the direction of convective flow compared to those surfaces against the main flow steam. The boiling heat transfer characteristics of subcooled flow were dominated by surface wettability, the pillar spacing, and the wicking direction; herein, boiling heat transfer was primarily influenced by pillar deflection. Among the test surfaces, the hydrophilic surface with deflecting PDMS pillars spaced at 250 μm on a silicon substrate was optimal.

4. Conclusions

Anisotropic wicking surfaces of deflected PDMS pillars (average tilt angle 30°) that varied in terms of between-pillar spacing directionally manipulated rewetting and considerably improved the CHF and the HTC during subcooled flow. We explored the chemical and structural effects of surface wettability, pillar spacing, and unidirectional wicking characteristics on boiling heat transfer at 40 K of subcooling. We measured heat transfer, the surface wicking, and bubble parameters. Our key conclusions are:

1. The overall CHF and HTC on anisotropic wicking surfaces with varied pillar spacings were significantly greater than those on hydrophilic and hydrophobic bare PDMS surfaces (by 14–34 and 6–23% respectively).
2. Narrowing the pillar spacing from 500 to 250 μm promoted bubble nucleation and enhanced capillary pumping.
3. Capillary pumping was enhanced on hydrophilic surfaces when the pillars were deflected towards the direction of liquid propagation, but the liquid became pinned to the surface when the pillars were tilted against the flow direction. Thus, wicking was directionally dependent on surface wickability. The wicking velocities on surfaces with driving pillars spaced at 250 and 500 μm improved by 32 and 64% respectively.
4. Both hydrophilic and hydrophobic surfaces composed of deflecting pillars improved the CHF and were associated with relatively low force ratios (F_p:F_d) in the driving compared to the pinning direction; the enhancements in the CHF were 6–9% and 29–31% respectively.
5. Of anisotropic wicking surfaces, the hydrophilic surface featuring deflecting pillars spaced at 250 μm were optimal, which afforded the highest boiling heat transfer performance during subcooled flow. Our experimental results and analysis of the relationship between the force ratio on anisotropic wicking surfaces, and the relative boiling characteristics, can be used to optimize anisotropic wicking for improving boiling heat transfer.

Acknowledgement

This work was supported by the Human Resources Development program (No.20204030200110) of the Korea Institute of Energy Technology Evaluation and Planning(KETEP) grant funded by the Korea government Ministry of Trade, Industry and Energy.

Declaration of Competing Interest

The authors declare no competing financial interest.

References

[1] Al-Karaghouli, A., Kazmerski, L.L. Energy consumption and water production cost of conventional and renewable-energy-powered desalination processes. Renewable and Sustainable Energy Reviews **24**, 343–356 (2013).

[2] Liu, H., Zhang, X., Quan, L., Zhang, H. Research on energy consumption of injection molding machine driven by five different types of electro-hydraulic power units. Journal of Cleaner Production **242**, 118355 (2020).

[3] Lasance, Technical data column, Electronics cooling, **3** (1997).

[4] Ishii, D., Horiguchi, H., Hirai, Y., Yabu, H., Matsuo, Y., Ijiro, K., Tsujii, K., Shimozawa, T., Hariyama, T., Shimomura, M., 2013. Water transport mechanism through open capillaries analyzed by direct surface modifications on biological surfaces. *Scientific Reports* **3**, 3024 (2013).

[5] Tani, M., Ishii, D., Ito, S., Hariyama, T., Shimomura, M., Okumura, K., 2014. Capillary Rise on Legs of a Small Animal and on Artificially Textured Surfaces Mimicking Them. *PLOS ONE* **9**, (2014).

[6] Hao, L., Fu, X., Li, T., Zhao, N., Shi, X., Cui, F., Du, C., Wang, Y., 2016. Surface chemistry from wettability and charge for the control of mesenchymal stem cell fate through self-assembled monolayers. *Colloids and Surfaces B: Biointerfaces* **148**, 549–556 (2016).

[7] Zhang, T., Lin, P., Wei, N., Wang, D., 2020. Enhanced Photoelectrochemical Water-Splitting Property on TiO2 Nanotubes by Surface Chemical Modification and Wettability Control. *ACS Appl. Mater.* Interfaces **12**, 20110–20118 (2020).

[8] Chen, Z., Li, W., Li, J., Zhou, K. & Feng, Z. A New Correlation for Subcooled Flow Boiling Heat Transfer in a Vertical Narrow Microchannel. *Journal of Electronic Packaging* **143** (2020).

[9] Cheng, H.-C., Jiang, Z.-X., Chang, T.-L. & Chen, P.-H. Effects of difference in wettability level of biphilic patterns on copper tubes in pool boiling heat transfer. *Experimental Thermal and Fluid Science* **120**, 110241 (2021).

[10] Coyle, C., O'Hanley, H., Phillips, B., Buongiorno, J. & McKrell, T. Effects of Hydrophobic Surface Patterning on Boiling Heat Transfer and Critical Heat Flux of Water at Atmospheric Pressure. *ASME* (2013).

[11] Allred, T. P., Weibel, J. A. & Garimella, S. V. Enabling Highly Effective Boiling from Superhydrophobic Surfaces. *Phys. Rev. Lett.* **120**, 174501 (2018).

[12] Wen, R., Xu, S., Lee, Y.-C. & Yang, R. Capillary-driven liquid film boiling heat transfer on hybrid mesh wicking structures. *Nano Energy* **51**, 373–382 (2018).

[13] Kim, B. S., Choi, G., Shim, D. I., Kim, K. M. & Cho, H. H. Surface roughening for hemi-wicking and its impact on convective boiling heat transfer. *International Journal of Heat and Mass Transfer* **102**, 1100–1107 (2016).

[14] Cao, L., Zhu, W., Luo, B., Miao, M., Wang, L., Zhang, H., Deng, Y. Construction of Core–Shell Nanowire Arrays in a Cu–Cu2O Film Electrode for High Efficiency in Heat Dissipation. ACS Appl. Mater. Interfaces 12, 3836–3846 (2020).

[15] Wang, S., Chen, H.-H. & Chen, C.-L. Enhanced flow boiling in silicon nanowire-coated manifold microchannels. *Applied Thermal Engineering* **148**, 1043–1057 (2019).

[16] Hsu, W.-T., Lee, D., Lee, N., Yun, M. & Cho, H. H. Enhancement of flow boiling heat transfer using heterogeneous wettability patterned surfaces with varying inter-spacing. *International Journal of Heat and Mass Transfer* **164**, 120596 (2021).

[17] Rahman, M. M., Ölçeroğlu, E. & McCarthy, M. Role of Wickability on the Critical Heat Flux of Structured Superhydrophilic Surfaces. *Langmuir* **30**, 11225–11234 (2014).

[18] Song, Y., Gong, S., Vaartstra, G., Wang, E.N. Microtube Surfaces for the Simultaneous Enhancement of Efficiency and Critical Heat Flux during Pool Boiling. ACS Appl. Mater. Interfaces **13**, 12629–12635 (2021).

[19] Chung, J. Y., Youngblood, J. P. & Stafford, C. M. Anisotropic wetting on tunable micro-wrinkled surfaces. *Soft Matter* **3**, 1163–1169 (2007).

[20] Parihar, V., Bandyopadhyay, S., Das, S., Dasgupta, S. Anisotropic Electrowetting on Wrinkled Surfaces: Enhanced Wetting and Dependency on Initial Wetting State. Langmuir **34**, 1844–1854 (2018).

[21] Bliznyuk, O., Jansen, H. P., Kooij, E. S., Zandvliet, H. J. W. & Poelsema, B. Smart Design of Stripe-Patterned Gradient Surfaces to Control Droplet Motion. *Langmuir* **27**, 11238–11245 (2011).

[22] Chun, J., Xu, C., Zhang, Y., Li, Q., Wen, R., Ma, X., 2021. Fast Capillary Wicking on Hierarchical Copper Nanowired Surfaces with Interconnected V-Grooves: Implications for Thermal Management. ACS Appl. Nano Mater. **4**, 5360–5371 (2021).

[23] Yu, N., Wang, S., Liu, Y., Xue, P., Ge, P., Nan, J., Ye, S., Liu, W., Zhang, J., Yang, B., 2017. Thermal-Responsive Anisotropic Wetting Microstructures for Manipulation of Fluids in Microfluidics. *Langmuir* **33**, 494–502 (2017).

[24] Meng, X., Yang, J., Liu, W., Ramakrishna, S., Sun, Y., Dai, Y. Stimulus-Responsive Graphene with Periodical Wrinkles on Grooved Microfiber Arrays: Simulation, Programmable Shape-Shifting, and Catalytic Applications. ACS Appl. Mater. Interfaces **13**, 26561–26572 (2021).

[25] Chu, K.-H., Xiao, R. & Wang, E. N. Uni-directional liquid spreading on asymmetric nanostructured surfaces. *Nature Materials* **9**, 413–417 (2010).

[26] Chen, C.-M. & Yang, S. Directed Water Shedding on High-Aspect-Ratio Shape Memory Polymer Micropillar Arrays. *Advanced Materials* **26**, 1283–1288 (2014).

[27] Akasaka, T., Miyaji, H., Imamura, T., Kaga, N., Yokoyama, A., Yoshida, Y., 2017. SUBMICRO-PATTERNING OF CURABLE DENTAL MATERIALS BY MOLDING METHODS : A SCREENING TRIAL. *Digest Journal of Nanomaterials and Biostructures* **12**, 281–292 (2017).

[28] Barreau, V., Yu, D., Hensel, R. & Arzt, E. Elevated temperature adhesion of bioinspired polymeric micropatterns to glass. *Journal of the Mechanical Behavior of Biomedical Materials* **76**, 110–118 (2017).

[29] Lakshminarayanan, S. Micro/Nano Patterning on Polymers Using Soft Lithography Technique. *Micro/Nanolithography - A Heuristic Aspect on the Enduring Technology* (2017).

[30] Kim, B.S., Shin, S., Lee, D., Choi, G., Lee, H., Kim, K.M., Cho, H.H., 2014. Stable and uniform heat dissipation by nucleate-catalytic nanowires for boiling heat transfer. *International Journal of Heat and Mass Transfer* **70**, 23–32 (2014).

[31] Lee, D., Kim, B.S., Moon, H., Lee, N., Shin, S., Cho, H. H., 2018. Enhanced boiling heat transfer on nanowire-forested surfaces under subcooling conditions. *International Journal of Heat and Mass Transfer* **120**, 1020–1030 (2018).

[32] Lee, D., Lee, N., Hsu, W.-T., Yun, M. & Cho, H. H. Enhanced boiling heat transfer on micro-structured surfaces via ultrasonic actuation. *International Communications in Heat and Mass Transfer* **113**, 104512 (2020).

[33] Chu, K.-H., Enright, R. & Wang, E. N. Structured surfaces for enhanced pool boiling heat transfer. *Appl. Phys. Lett.* **100**, 241603 (2012).

[34] Zhu, Y., Antao, D.S., Chu, K.-H., Chen, S., Hendricks, T.J., Zhang, T., Wang, E.N., 2016. Surface Structure Enhanced Microchannel Flow Boiling. *Journal of Heat Transfer* **138**, 091501 (2016).

[35] Kuan, W.K., and Kandlikar, S. G., "Critical heat flux measurement and model for refrigerant-123 under stabilized flow conditions in micro channels," *ASME. Heat transfer*, **130**(3), p. 034503 (2008).

[36] Shin, S., Choi, G., Kim, B. S. & Cho, H. H. Flow boiling heat transfer on nanowire-coated surfaces with highly wetting liquid. *Energy* **76**, 428–435 (2014).

[37] Malvadkar, N. A., Hancock, M. J., Sekeroglu, K., Dressick, W. J. & Demirel, M. C. An engineered anisotropic nanofilm with unidirectional wetting properties. *Nature Materials* **9**, 1023–1028 (2010).

Table Captions

Table 1. The details of the deflecting PDMS-based pillar surfaces.

Table 2. The dynamic contact angles on test surfaces.

Table 1 The details of the deflecting PDMS-based pillar surfaces

Surface wettability	Spacings between pillars [μm]	Alignment	Averaged tilting angle [°]	Diameter [μm]	Height [μm]
Hydrophobic	250	Deflecting	30	50	300
Hydrophobic	500	Deflecting	30	50	300
Hydrophilic	250	Deflecting	30	50	300
Hydrophilic	500	Deflecting	30	50	300

Table 2 The dynamic contact angles on test surfaces

Bare PDMS			
Hydrophilic		Hydrophobic	
α [°]	β [°]	α [°]	β [°]
65 ±1.3	45 ±0.8	99 ±1.5	75 ±1.1

P250							
Hydrophilic				Hydrophobic			
Toward		Against		Toward		Against	
α [°]	β [°]	α [°]	β [°]	α [°]	β [°]	α [°]	β [°]
33 ±0.8	15 ±0.3	70 ±0.6	53 ±0.4	92 ±0.7	81 ±0.5	99 ±0.6	87 ±0.5

Figure Captions

Figure 1. A schematic of the effects of wicking direction on anisotropic wicking during subcooled flow boiling.

Figure 2 (a) Fabrication process of vertical PDMS pillar arrays on silicon substrates(b) A schematic of pillar bending to 30^{o}via sputter coating. (c) Scanning electron microscopy (SEM) images of surfaces with bent pillar arrays spaced at 250 and 500 μm.

Figure 3. (a) PDMS stamps on a silicon substrate. (b) The several layers lying between the polymerized pillar arrays and the silicon substrates. (c) PDMS pillars with 200-nm-thick SiO_2 coatings. (d) The apparent surface contact angles of various PDMS surfaces.

Figure 4. (a) Evaluation of subcooled flow boiling. (b) A resistance temperature detector (RTD) sensor. (c) Copper bus bars loading on chemically coating layers consisted of Au electrodes and ITO heater. (d) Location of temperature components in the flow channel.

Figure 5 Flow boiling characteristics under the subcooled 40 K condition. The relationship between heat flux and the extent of subcooling for hydrophilic (a) and (b) hydrophobic PDMS surfaces. (c) The HTCs of anisotropic wicking surfaces by surface wettability and the directions of the deflecting pillars.

Figure 6. The relationships between the CHF and apparent surface contact angles (surface wettabilities) of various PDMS surfaces.

Figure 7. Wicking of hydrophilic polymerized surfaces with tilted pillar arrays spaced at (a) 250 μm and 500 μm. (b) The effects of pillar bending direction on the relative wicking characteristics of polymerized test surfaces composed of hydrophilic tilted pillar arrays spaced at 250 and 500 μm.

Figure 8. A schematic showing the effect of wicking direction on subcooled, flow boiling heat transfer.

Figure 9. (a) Measurement of dynamic contact angles on bare PDMS test surfaces and surfaces with bending pillar arrays spaced at 250 μm (b) F_{pin}:F_{rel} force ratio as a function of receding contact angles of test surfaces predicted using dynamic contact angles measured on bare PDMS surfaces and bending pillar surfaces with 250-μm spcing.

Figure 10. The CHF as a function of the F_{pin}:F_{rel} force ratio in terms of the influence of the pillar tilting direction of polymerized test surfaces on subcooled, flow boiling heat transfer.

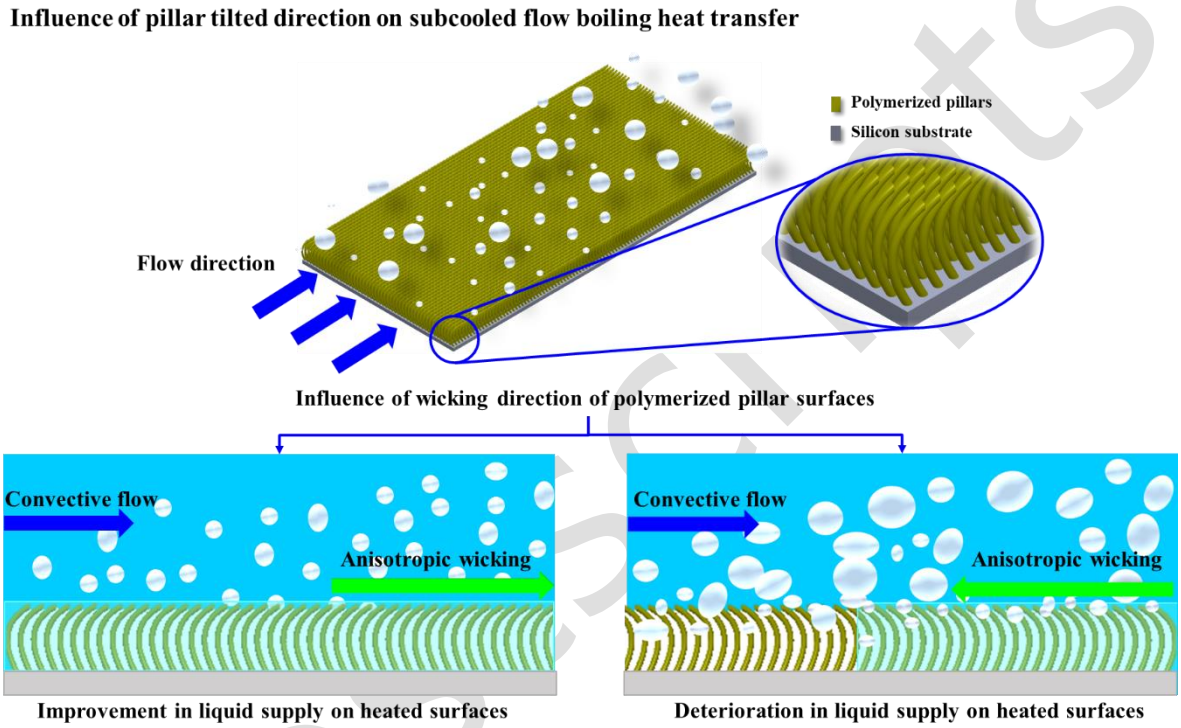

Fig. 1 A schematic of the effects of wicking direction on anisotropic wicking during subcooled flow boiling.

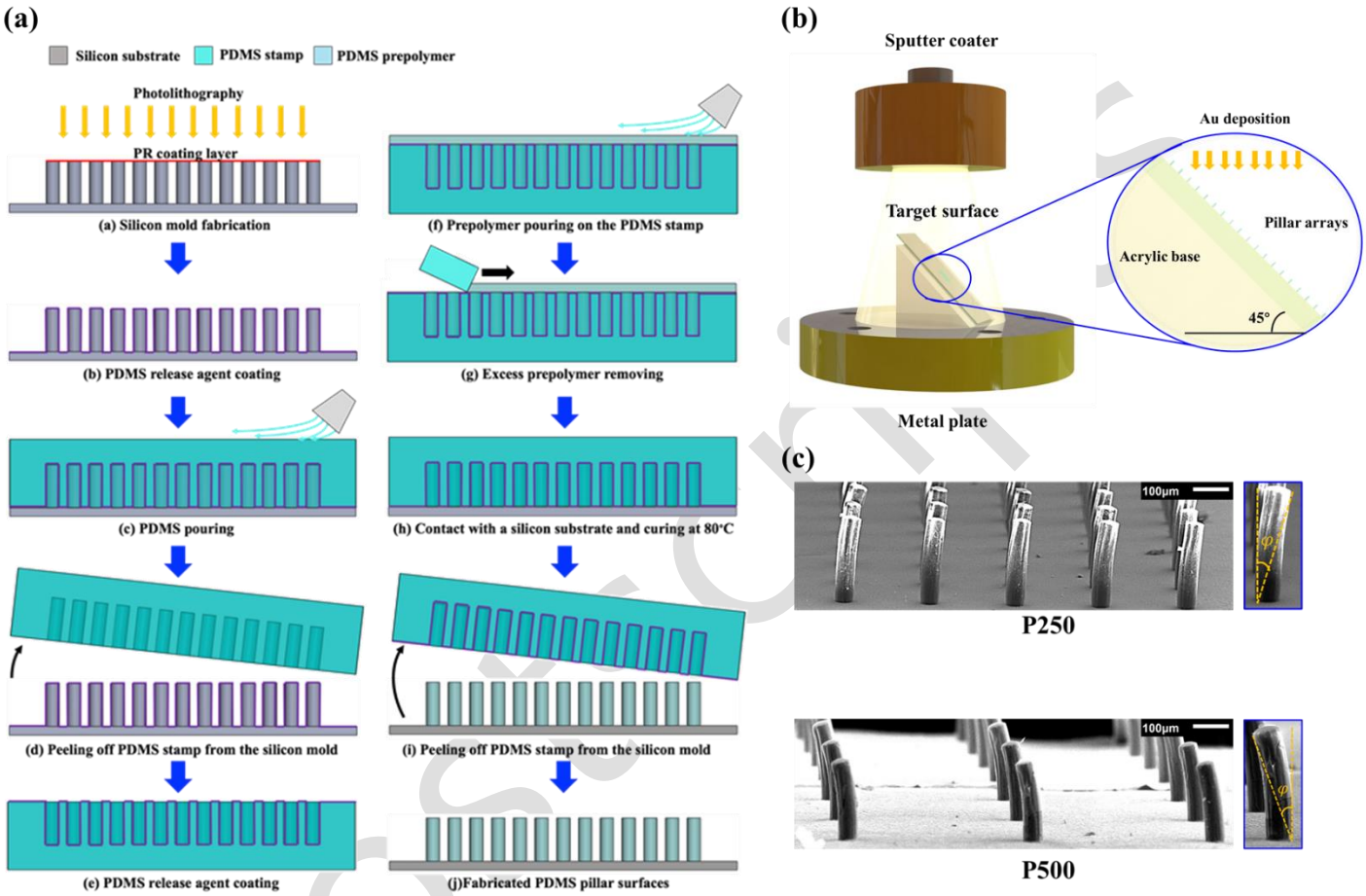

Fig. 2 (a) Fabrication process of vertical PDMS pillar arrays on silicon substrates(b) A schematic of pillar bending to 30°via sputter coating. (c) Scanning electron microscopy (SEM) images of surfaces with bent pillar arrays spaced at 250 and 500 μm.

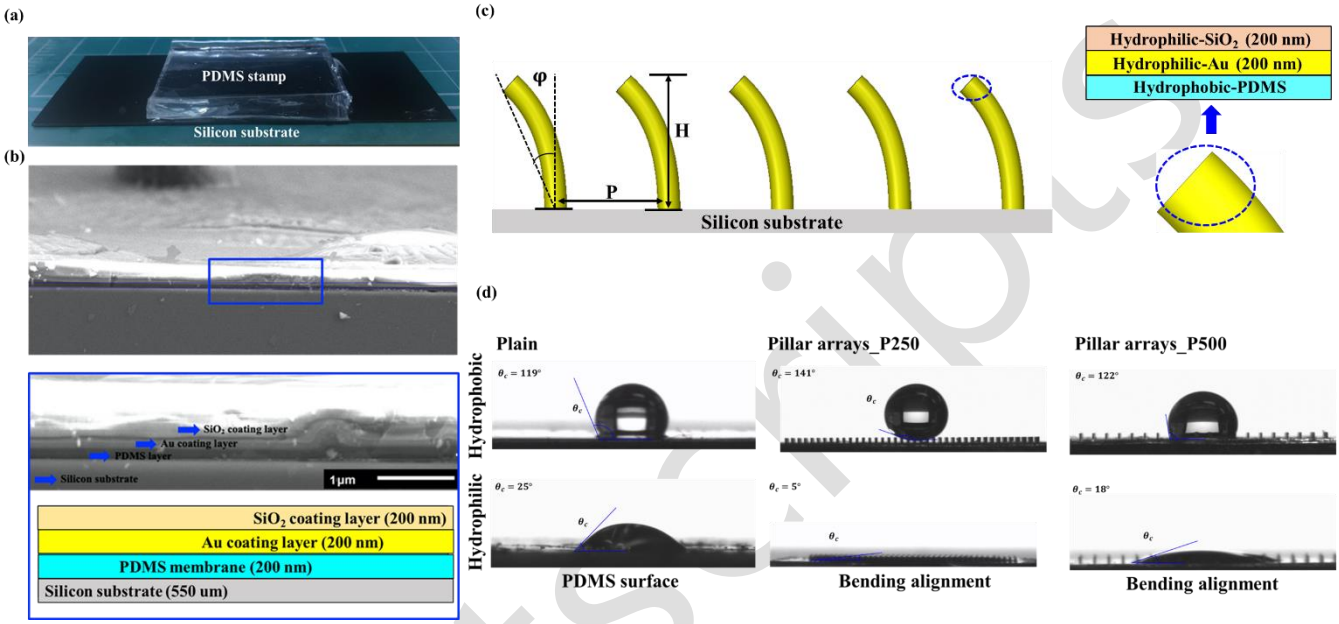

Fig. 3 (a) PDMS stamps on a silicon substrate. (b) The several layers lying between t he polymerized pillar arrays and the silicon substrates. (c) PDMS pillars with 200-nm-thick SiO_2 coatings. (d) The apparent surface contact angles of various PDMS surface s.

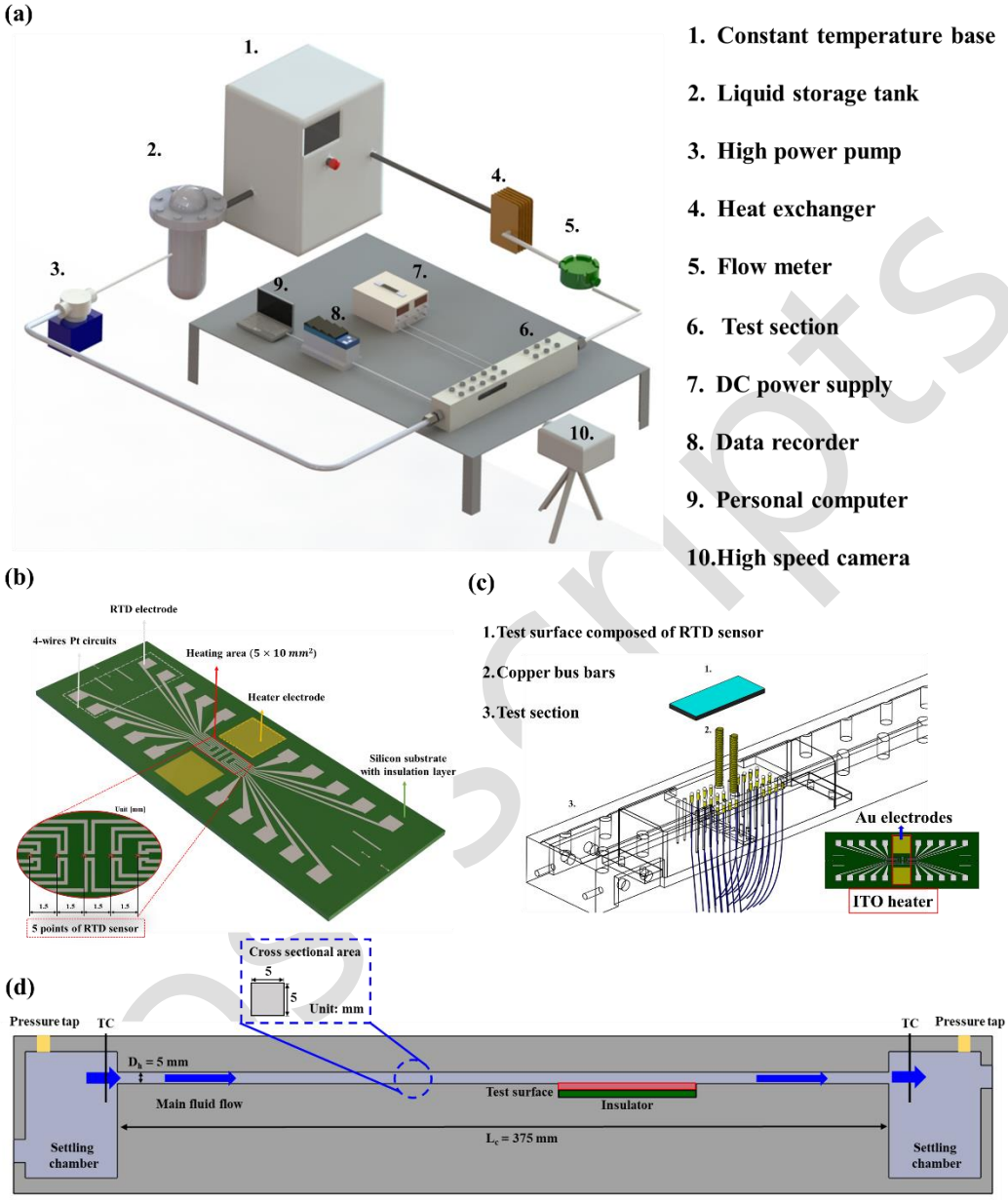

Fig. 4 The experimental setup. (a) Evaluation of subcooled flow boiling. (b) A resistance temperature detector (RTD) sensor. (c) Copper bus bars loading on chemically coating layers consisted of Au electrodes and ITO heater. (d) Location of temperature components in the flow channel.

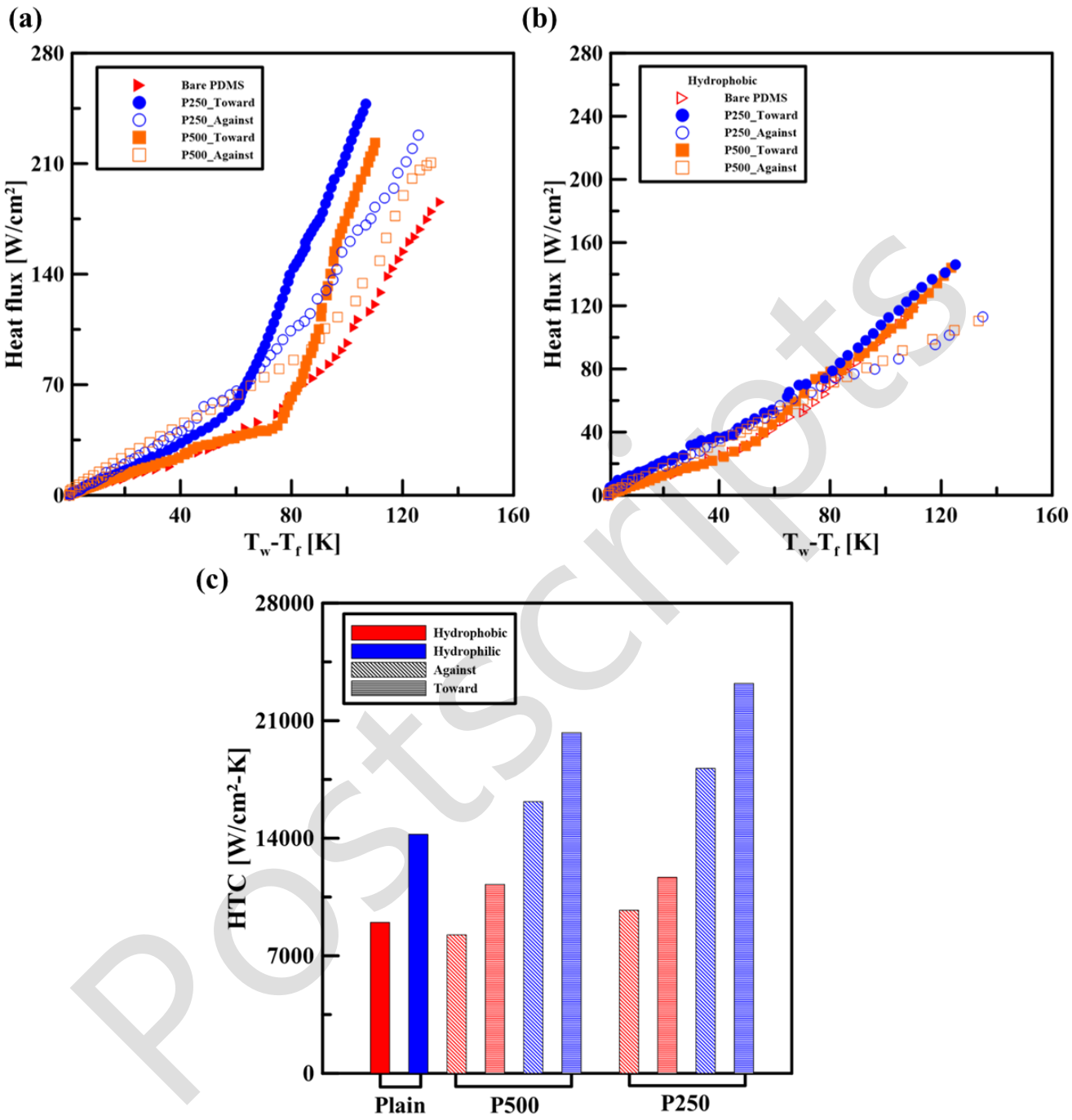

Fig. 5 Flow boiling characteristics under the subcooled 40 K condition. The relationship between heat flux and the extent of subcooling for hydrophilic (a) and (b) hydrophobic PDMS surfaces. (c) The HTCs of anisotropic wicking surfaces by surface wettability and the directions of the deflecting pillars.

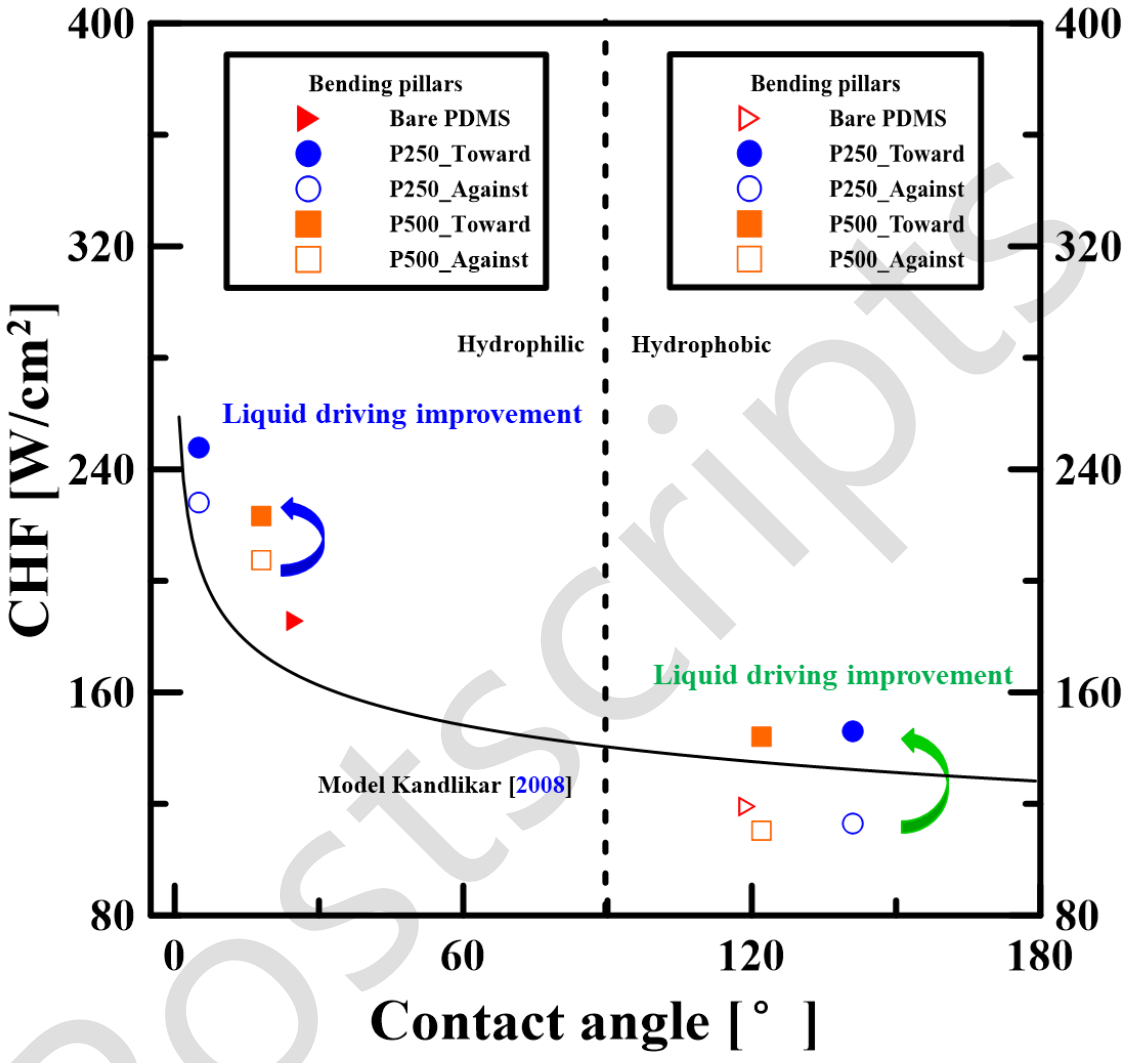

Fig. 6 The relationships between the CHF and apparent surface contact angles (surface wettabilities) of various PDMS surfaces.

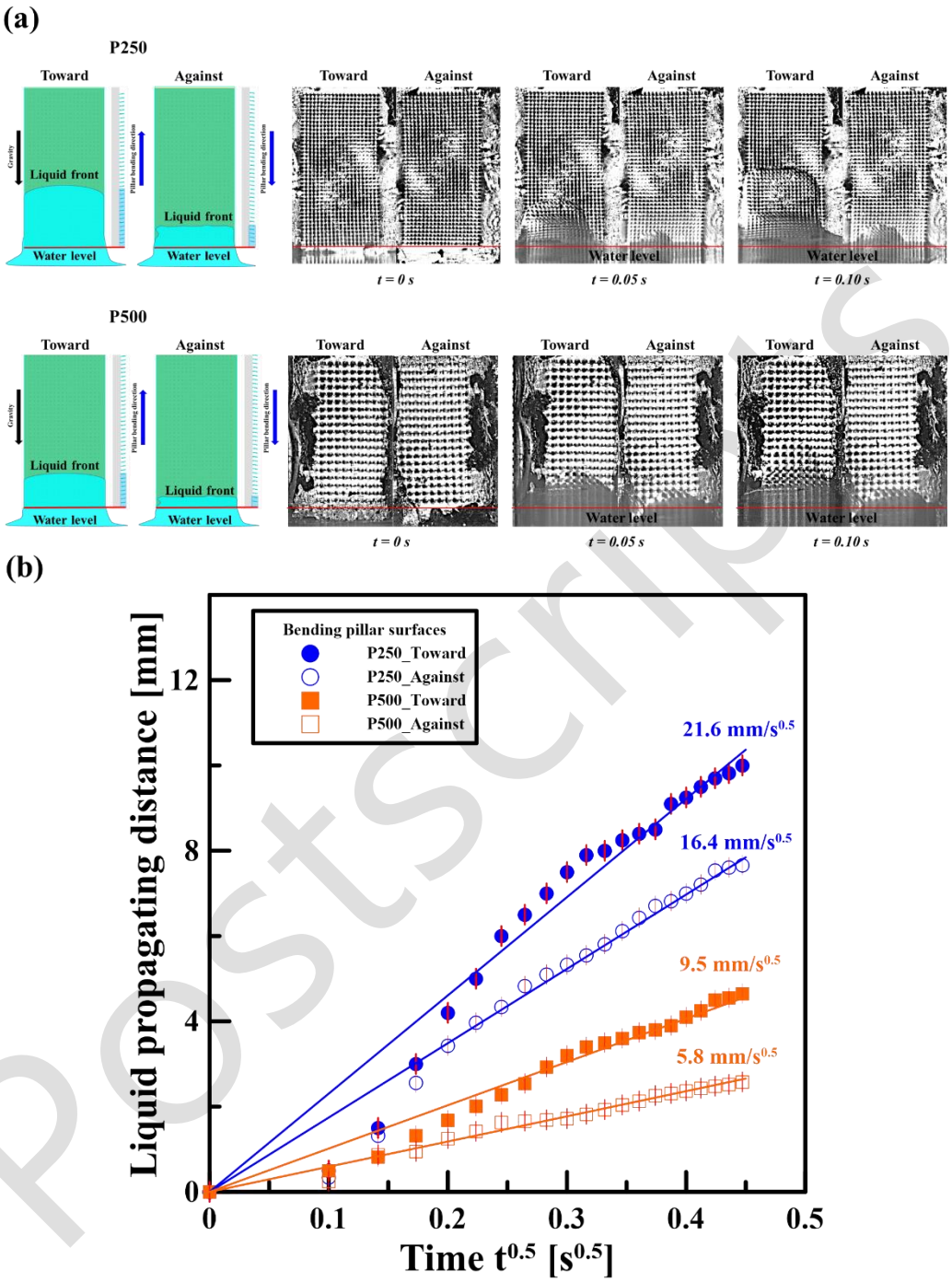

Fig. 7 Wicking of hydrophilic polymerized surfaces with tilted pillar arrays spaced at (a) 250 μm and 500 μm. (b) The effects of pillar bending direction on the relative wicking characteristics of polymerized test surfaces composed of hydrophilic tilted pillar arrays spaced at 250 and 500 μm.

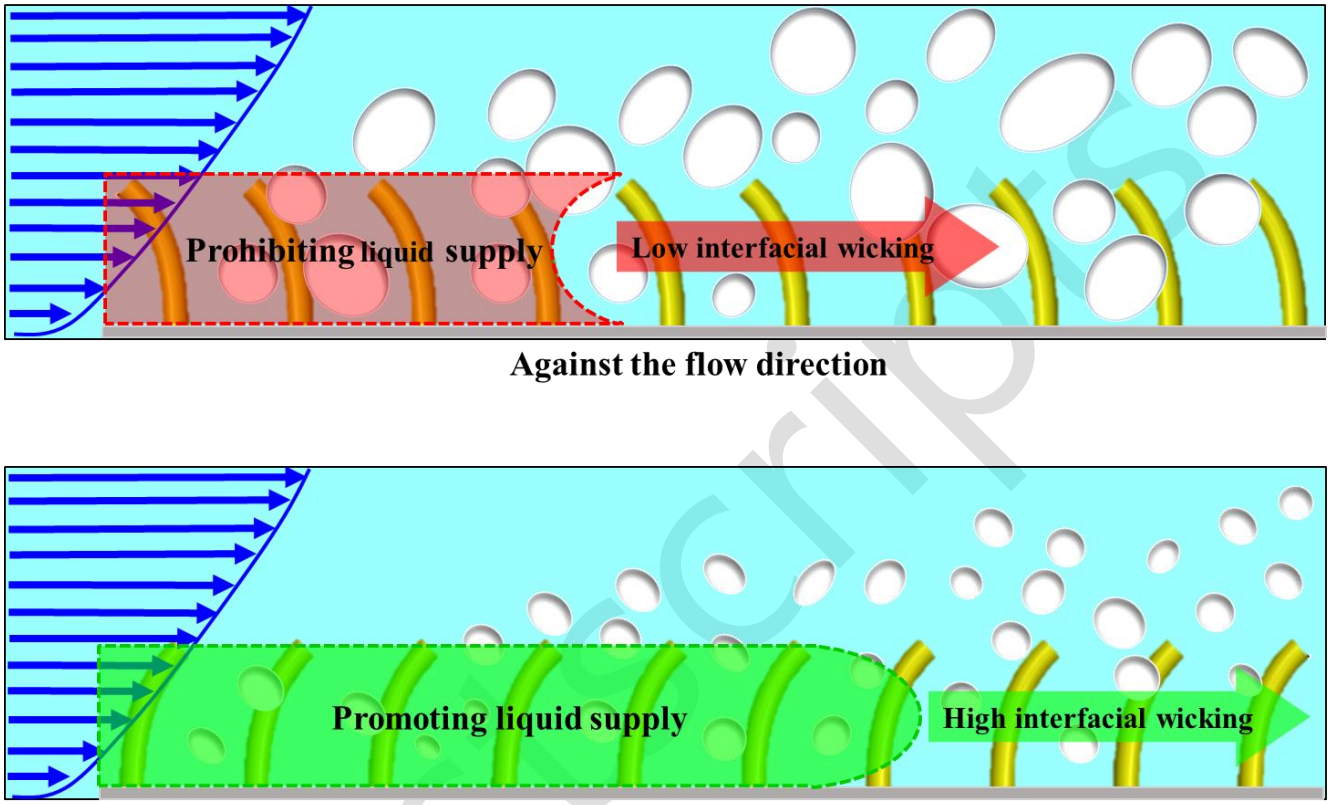

Fig. 8 A schematic showing the effect of wicking direction on subcooled, flow boiling heat transfer.

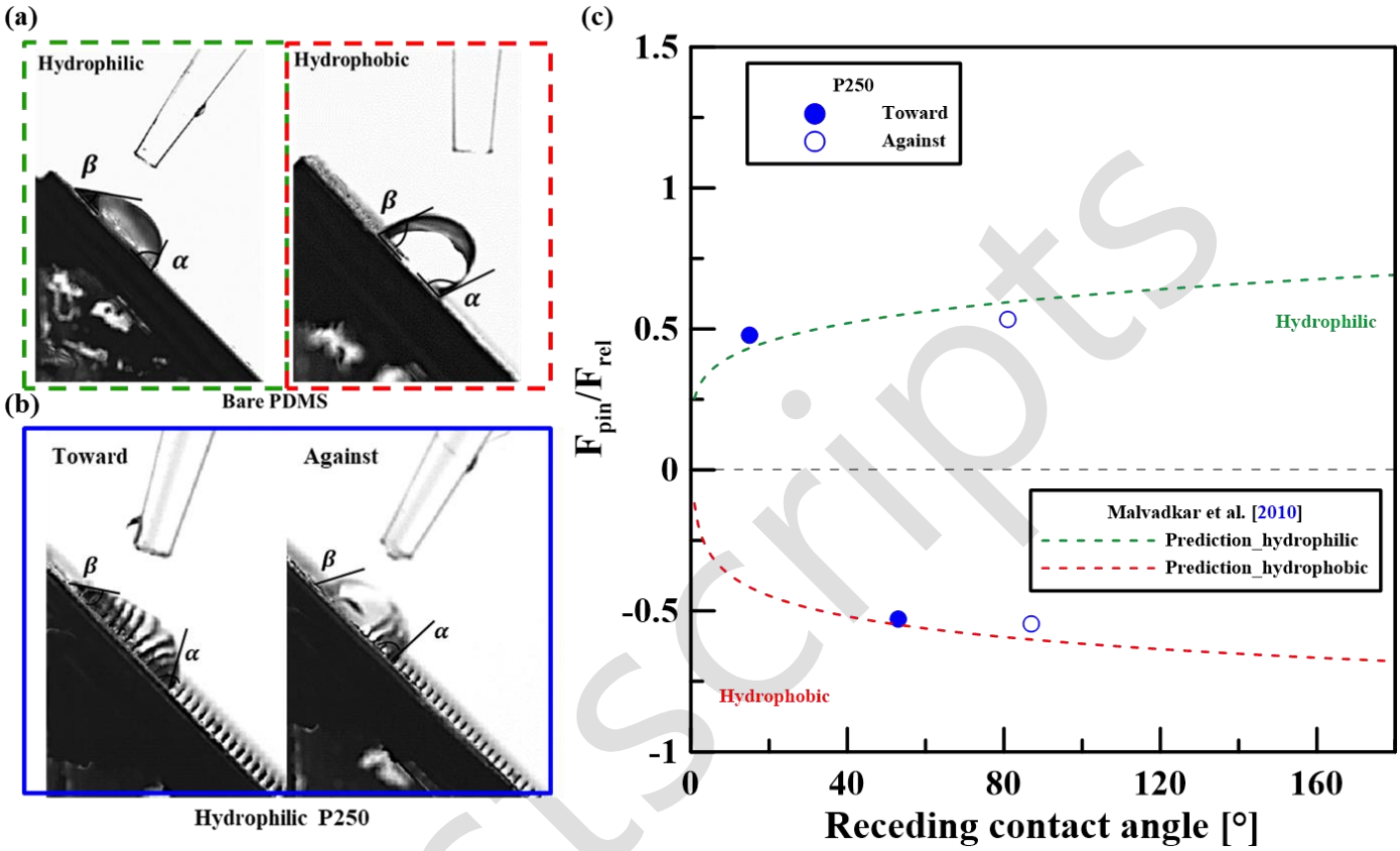

Fig. 9 (a) Measurement of dynamic contact angles on bare PDMS test surfaces and surfaces with bending pillar arrays spaced at 250 μm (b) F_{pin}:F_{rel} force ratio as a function of receding contact angles of test surfaces predicted using dynamic contact angles measured on bare PDMS surfaces and bending pillar surfaces spaced at 250 μm.

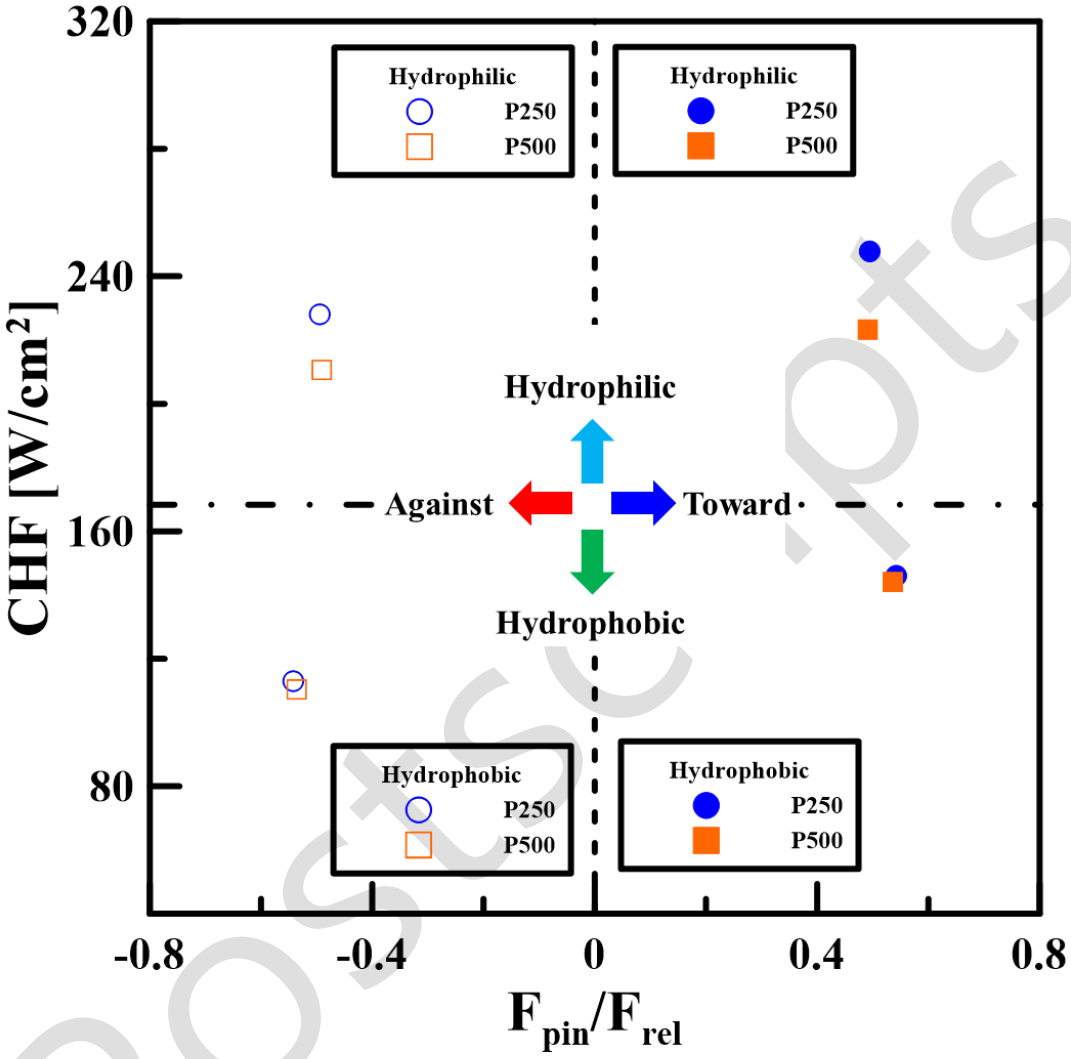

Fig. 10 The CHF as a function of the F_{pin}:F_{rel} force ratio in terms of the influence of the pillar tilting direction of polymerized test surfaces on subcooled, flow boiling heat transfer.